

Patterns of electroconvection in the nematic liquid crystal N4

Denis Funfschilling, Brian Sammuli, and Michael Dennin

Department of Physics and Astronomy, University of California, Irvine, Irvine, California 92696-4575

(Received 10 September 2002; published 16 January 2003)

Electroconvection using the liquid crystal N4 is studied as a function of two control parameters: the applied frequency and the applied voltage. As a function of voltage, there is a rich series of bifurcations that takes the system from stationary rolls to chaos. As a function of the frequency, the initial pattern changes from stationary oblique rolls at low frequencies to stationary normal rolls at higher frequencies. There is also a change in the secondary bifurcations. In particular, we observe that the bimodal-varicose instability is replaced by the skewed-varicose instability as the applied frequency is increased. Comparisons with theoretical predictions are made.

DOI: 10.1103/PhysRevE.67.016207

PACS number(s): 47.54.+r, 47.20.-k, 61.30.-v

I. INTRODUCTION

When spatially extended systems are driven out of equilibrium, there typically exists a critical value of the driving force where the system makes a transition from a uniform state to a periodic state, or pattern [1]. One can consider two broad classes of spatially extended systems: isotropic and anisotropic. Nematic liquid crystals have proven extremely useful for the study of pattern formation in anisotropic systems [2]. A nematic liquid crystal is a rodlike molecule that possesses orientational order, but no spatial order [3]. The average alignment of the molecules is referred to as the director. By preparing samples where the director is spatially uniform, a preferred spatial direction is selected. Of the various examples of pattern formation in nematic liquid crystals, electroconvection has proven particularly fruitful.

For electroconvection, a nematic liquid crystal is confined between two plates and a voltage is applied between the plates. For planar alignment of the director (i.e., the director parallel to the plates), a rich variety of patterns have been observed, including traveling waves [4–7], defect mediated chaos [5,8], localized states [9–11], abnormal rolls [12,13], grid patterns [14], bimodal-varicose state [15–17], and spatiotemporal chaos at onset [18–20]. Many of these patterns are superpositions of, or variations of, an important class of patterns that is not present in isotropic systems: oblique rolls. Oblique rolls are a pattern of straight rolls that have a non-zero angle between the wave vector of the pattern and the undistorted director. (There is also a growing body of work on homeotropically aligned convection, but that is beyond the scope of this paper [2].)

One of the successes of electroconvection has been the ability of theory to quantitatively describe much of the pattern forming phenomena, despite the complexity of the fundamental equations required to describe electroconvection [16,21,22]. Because the system is anisotropic, most of the material parameters are tensor quantities. Therefore, a theoretical description of electroconvection involves at least 12 different material parameters, many of which are difficult to measure directly. Despite successes in various regions of parameter space [22,16], a complete theory of electroconvection that explains all of the phenomena has not been formulated. Two important phenomena that are described

separately are the traveling rolls states found at low conductivity [7,22] and the abnormal rolls and bimodal-varicose instability present in stationary states [12,16,23]. Recent work in Rayleigh-Bénard convection with nematic liquid crystals and in electroconvection has provided a solid framework for a qualitative understanding of the abnormal rolls and bimodal-varicose instability. This work treats a twist mode of the director as a dynamically active mode [23,24]. However, more quantitative work, especially comparison between experiment and theory, is needed in this area.

In this paper, we report results for electroconvection in the liquid crystal Merck N4. We present a pattern state diagram for the material for use in guiding future experiments. Many of the patterns that we observe are well known, and have been observed with other liquid crystals, such as MBBA, phase V, and I52. However, there are some unique features of the pattern state diagram that suggest interesting future experiments with this material. The rest of the paper is organized as follows. Section II describes the experimental setup and techniques. Also, the physical properties of the N4 cells are presented in Sec. II. In Sec. III, we present the pattern state diagram and the different patterns found for electroconvection in N4. Finally, Sec. IV summarizes the results.

II. EXPERIMENTAL DETAILS

The N4 liquid crystal is a eutectic mixture of two azoxy compounds, $\text{CH}_3\text{O}-\text{C}_6\text{H}_4-\text{NO}=\text{N}-\text{C}_6\text{H}_4-\text{C}_4\text{H}_9$ and $\text{CH}_3\text{O}-\text{C}_6\text{H}_4-\text{N}=\text{NO}-\text{C}_6\text{H}_4-\text{C}_4\text{H}_9$. Some of the known properties of N4 are as follows. N4 has a clearing point of 76°C . Its dielectric anisotropy is $\Delta\varepsilon = \varepsilon_{\parallel} - \varepsilon_{\perp} = -0.2$, and its optical anisotropy is $\Delta n = n_{\parallel} - n_{\perp} = 0.28$ [25]. We measured K_{33} in a homeotropically aligned cell specially built for this purpose. The critical voltage of the Fredricks bend transition was $V_c^F = 9.3$ V at 30°C . Since $V_c^F = \pi(K_{33}/(\varepsilon_a\varepsilon_o))^{1/2}$, this gives $K_{33} = 15.5 \times 10^{-12}$ N. This value is consistent with recent measurements reported in Ref. [26]. They report a value of $K_{33} = 1.29 \times 10^{-11}$ N and $K_{11}/\chi_a = 2.0 \times 10^{-4}$ G^2m^2 at a temperature of 25°C [26]. The shear viscosity is $\mu = 30 \times 10^{-3}$ Pa s [25] at 20°C , and the rotational viscosity is $\gamma_1 = 0.1204$ Pa s [27].

For our experiments, N4 is doped with 0.1 wt% of tetra *n*-butylammonium bromide $[(\text{C}_4\text{H}_9)_4\text{NBr}]$. The N4/

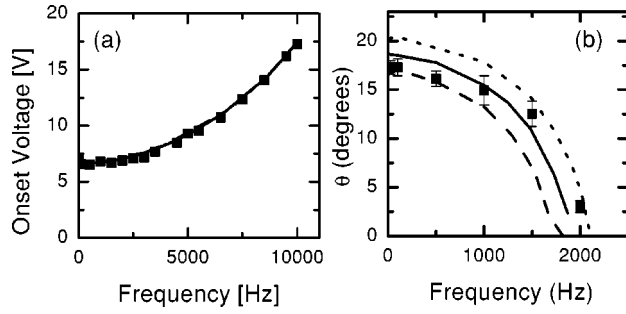


FIG. 1. (a) The onset voltage as a function of applied frequency. (b) The critical angle θ as a function of applied frequency. In both plots, the symbols are the measured points. The solid curve is computed using the parameters in Table I. The dashed curve uses the parameters listed in Table I, but with $k_{22}=5.11 \times 10^{-12}$ N. The dotted curve uses the parameters listed in Table I, but with $k_{22}=5.31 \times 10^{-12}$ N.

bromide solution is stirred at room temperature for a few days to a week to ensure that the tetra *n*-butylammonium bromide is completely dissolved. Before filling a cell, the N4 solution is filtered by a syringe filter of 0.45- μm pore size.

The electrical conductivity of the cell is measured by applying an ac voltage across the cell and measuring the amplitude and the phase of the resulting current. We used a current to voltage converter as described in Ref. [28] and digitized the voltage signal in the computer. The in-phase and out-of-phase components of the resulting current were computed using sine and cosine transforms. They provided both the resistance and the capacitance of the cell. Knowing the geometry, the resistance was converted to conductivity. In particular, given our geometry, we measure the perpendicular conductivity σ_{\perp} . σ_{\perp} was temperature, and weakly frequency, dependent. The conductivity of our doped N4 is relatively high compared to other standard solutions used for electroconvection. For comparison, a typical range for N4 is $3 \times 10^{-7} \leq \sigma_{\perp} \leq 3 \times 10^{-6} \Omega^{-1} \text{m}^{-1}$. For I52 [7], $1 \times 10^{-9} \leq \sigma_{\perp} \leq 1 \times 10^{-8} \Omega^{-1} \text{m}^{-1}$. For Merck phase 5 [9], $\sigma_{\perp} = 4.4 \times 10^{-8} \Omega^{-1} \text{m}^{-1}$. Two weeks after the end of the experiment, the conductivity measured in our cell was $\sigma_{\perp} = 1.3 \times 10^{-6} \Omega^{-1} \text{m}^{-1}$ at 30 °C. By measuring the conductivity as a function of time, and accounting for the small measured linear drift, we found that during the

experiment the conductivity was approximately $\sigma_{\perp} = 1.6 \times 10^{-6} \Omega^{-1} \text{m}^{-1}$.

We also determined the various material parameters by comparing the onset properties, V_c and θ , to numerical calculations of the onset voltage [29]. Here V_c is the critical voltage for the onset of electroconvection and θ is the angle between the roll wave vector and the undistorted director at onset. To determine V_c and θ , the voltage is increased quasistatically in increments of $\Delta V = 0.01$ V. After each step, the system is equilibrated for 300 s. Figure 1 is a plot of V_c and θ versus applied frequency at $T = 30$ °C. The theoretical curves used the measured values of $\epsilon_{\perp} = 5.7$, $\epsilon_{\parallel} = 5.5$, and $\sigma_{\perp} = 1.6 \times 10^{-6} \Omega^{-1} \text{m}^{-1}$. For the other material parameters, we used Ref. [23] as a guide, and selected $\sigma_{\parallel} = 2.03 \times 10^{-6} \Omega^{-1} \text{m}^{-1}$. The values for the elastic and viscous coefficients are listed in Table I. For illustration, we show three theoretical curves that correspond to different choices of the material parameter K_{22} : 5.11×10^{-12} , 5.21×10^{-12} , and 5.31×10^{-12} N. Varying K_{11} or K_{33} has similar effects. First, one observes that V_c is relatively insensitive to small changes in many of the parameters. However, it provides strong limits on the conductivity. However, θ is more sensitive to the exact ratio of elastic constants and viscosities. Therefore, one can determine surprisingly good estimates for all of the standard material parameters from just these two curves and the measurement of a single elastic constant and viscosity to set the scale. For comparison, Table I also includes the material parameters reported in Ref. [30] for the liquid crystal Merck phase 5 (N4 is a mixture of two components among the four types of molecules that are part of phase 5) and reported in Ref. [23] for the liquid crystal N4. For the data reported in Ref. [23], since only nondimensional relations were used, we write them in terms of the measured value of $K_{33} = 15.5 \times 10^{-12}$ N and the value of $\alpha_1 = 0.1204$ Pa s given in Ref. [27]. As shown in Table I, the only change needed to the parameters as used in Ref. [23] is to use a nonzero α_1 . In Ref. [23], $\alpha_1 = 0 \times 10^{-3}$ N, and we find $\alpha_1 = -39 \times 10^{-3}$ N. This value is consistent with the value given in Ref. [30].

Many of the transitions will be discussed in term of the dimensionless control parameter $\epsilon = (V/V_c)^2 - 1$, where V_c is the threshold voltage at which that transition from the uniform state to a pattern occurs. V_c is defined separately for

TABLE I. List of material parameters. The values in the row labeled Fig. 1 were used to compute the theoretical curves in Fig. 1.

Source	Parameters					
	K_{11} (N)		K_{22} (N)		K_{33} (N)	
Phase 5	9.8×10^{-12}		4.6×10^{-12}		12.7×10^{-12}	
N4 Ref. [23]	10.36×10^{-12}		5.21×10^{-12}		15.5×10^{-12}	
Figure 1	10.36×10^{-12}		5.21×10^{-12}		15.5×10^{-12}	
	α_1 (Pa s)	α_2 (Pa s)	α_3 (Pa s)	α_4 (Pa s)	α_5 (Pa s)	α_6 (Pa s)
Phase 5	-39×10^{-3}	-109.3×10^{-3}	1.5×10^{-3}	56.3×10^{-3}	82.9×10^{-3}	-24.9×10^{-3}
N4 Ref. [23]	0×10^{-3}	-117.6×10^{-3}	2.76×10^{-3}	59×10^{-3}	87.2×10^{-3}	-30.4×10^{-3}
Figure 1	-46×10^{-3}	-117.6×10^{-3}	2.76×10^{-3}	59×10^{-3}	87.2×10^{-3}	-30.4×10^{-3}

each applied frequency. The voltage steps used to measure V_c correspond to steps in $\Delta\epsilon < 0.003$, depending on V_c . The voltage is always either increased monotonically from the nonpattern forming regime to the chaotic regime, or decreased monotonically from the chaotic regime to the uniform state.

A standard issue with electroconvection is the stability of the samples. Because one purpose of this work is to serve as a reference for the behavior of N4, it is important to make a few comments on potential problems. Despite being remarkably stable under most conditions, heating solutions in the oven at 50 °C accelerated the dissolution of the bromide but produced a darker yellow solution. Even with filtering, dark dust was evident in the cells made with this solution, and the electroconvection patterns were not reproducible. Similar problems occurred with solutions containing substantially higher bromide content. A high bromide content also resulted in “fragile” cells. These cells were susceptible to various problems whenever even a small dc voltage was temporarily applied to the cell. Most of the problems resulted in the cells being unusable for electroconvection studies. Therefore, it is critical to take care with the doping procedure.

Another common issue in electroconvection is the “aging” of cells with time. As mentioned, we did observe a slow decrease in the conductivity over time. The main result of this was slight increases in V_c at higher frequencies as the cutoff frequency for the material changed. However, on the time scale of the experiments reported here (one week) there was no observable change in the material properties of the sample.

Commercial cells from EHC Ltd. in Japan were used for the studies reported here. The cells are composed of two glass plates that are roughly an inch on a side. In the center of each glass slide is a square electrode that is 1 cm \times 1 cm. The glass slides are spaced 25 μ m apart. The surfaces of the electrodes are treated with a rubbed polymer, and the direction of rubbing provides the axis along which the director is aligned. We refer to that axis as the x axis, and the direction perpendicular to the rubbing is the y axis. The z axis is perpendicular to the glass plate. The cell is placed in an aluminum temperature controlled block. Unless otherwise stated, the temperature was set to 30 °C and was maintained constant at ± 2 mK.

The optical system is described in detail in Ref. [17], and for a detailed discussion of the analysis of the system, see Ref. [31]. It consists of a light source and polarizer below the cell and a $\lambda/4$ plate and second polarizer (analyzer) above the cell. For all of our experiments, except the observation of abnormal rolls, the polarizer is aligned along the rubbing direction. Therefore, the cell is illuminated with extraordinary light. After the cell, the light goes through a $\lambda/4$ plate oriented at 45° with respect to the polarizer, and the analyzer has the same orientation as the polarizer. Without the $\lambda/4$ plate, this is the standard shadowgraph setup [32] used to observe the director tilt in the x - z plane, i.e., the study of convection rolls patterns. With the addition of a $\lambda/4$ plate at 45°, the rolls still appeared clearly, but one also can distinguish a director twist in the x - y plane. Depending on the

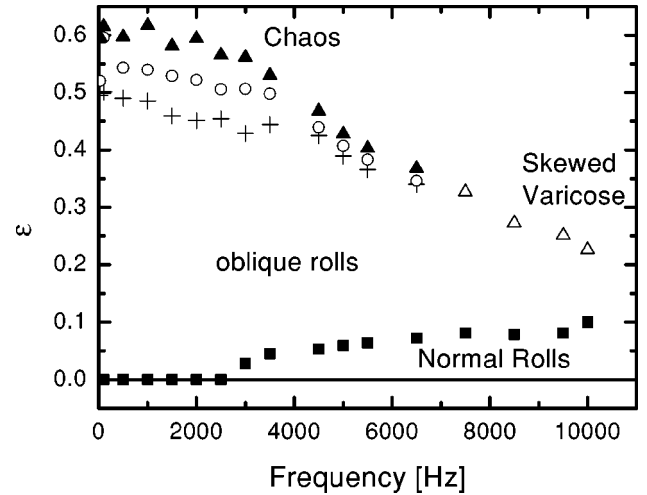


FIG. 2. Pattern state diagram of an N4 cell as a function of ϵ and frequency. The solid line is $\epsilon=0$. The symbols indicate the various transitions: (■) transition to oblique rolls, either directly from the uniform state or from normal rolls; (+) the bimodal-varicose instability; (○) the oscillatory bimodal-varicose instability; (▲) transition to chaotic state; and (△) skewed-varicose instability.

sense of the twist angle, a given region appears darker or lighter [31,32].

For a clearer observation of the twist mode in abnormal rolls, ordinary light (i.e., light polarized perpendicularly to the rubbing direction) is used. Again, the light coming out of the cell passes through a circular analyzer, i.e., a combination of a $\lambda/4$ plate oriented at 45° relative to the polarizer, and an analyzer oriented perpendicular to the polarizer direction. This setup is more sensitive to the director twist profile [17], but the roll structure is not visible [31]. In Ref. [31], the twist angle of dielectric rolls is calculated with this setup.

Images are taken by a monochrome CCD COHU camera with 640 \times 480 pixels and digitized with an eight-bit framegrabber. The resolution of the camera with this setup of the lenses is 375 pixel/mm. The images represent an area 1.28 mm \times 1.71 mm. Further image analysis and calculations are done with Matlab.

III. PATTERN STATE DIAGRAM

The pattern state diagram of N4 at 30 °C is presented in Fig. 2 in terms of ϵ versus frequency. As previously mentioned, ϵ is defined separately for each frequency in terms of the V_c at that frequency. The transitions were measured both by stepping up the voltage from below the initial onset to the fully chaotic regime and by stepping down the voltage from the chaotic regime to below onset. Within our resolution ($\Delta\epsilon \leq 0.005$), the transitions showed no hysteresis.

As expected, for low values of the applied frequency, the initial pattern is oblique rolls, and as the applied frequency is increased, the transition is to normal rolls. The frequency at which the initial transition switches from normal to oblique is referred to as the Lifshitz point. There were a number of different secondary bifurcations that we observed. In the ob-

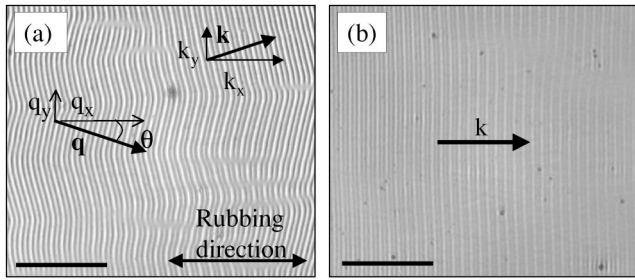


FIG. 3. Two images of the pattern at the onset of electroconvection. The solid bars in the lower left corner represent 0.5 mm. (a) Onset of zig and zag rolls at $V_{rms}=9.53$ V and a frequency of $f=500$ Hz. Also illustrated in the image is the definition of the x and y axis with respect to the undistorted director (rubbing direction). (b) Onset of normal rolls at $V_{rms}=10.76$ V and a frequency of $f=6500$ Hz.

lique roll state, we observed both the bimodal-varicose and skewed-varicose instabilities. This confirms the theoretical prediction that one can have a transition from the bimodal-varicose instability to the skewed-varicose instability. Further studies near the transition point will be interesting. From the bimodal-varicose state, we observed the onset of the oscillating bimodal-varicose state, and a further transition to a chaotic state. This chaotic state may simply be a more fully developed oscillating bimodal-varicose state. Finally, we observed the standard transition from normal rolls to oblique rolls via the zig-zag instability. Each transition will be discussed in more detail in the following paragraphs.

The initial bifurcation is to one of two states: oblique rolls or normal rolls. Images of the two states are shown in Fig. 3. The frequency at which there is a transition from oblique rolls at onset to normal rolls is known as the Lifshitz frequency. This can be seen in Fig. 1(b). Figure 4 shows the evolution of the modulus of the wave vector and the angle θ between the wave vector and the rubbing direction for a frequency below the Lifshitz frequency (100 Hz). Above the Lifshitz point, there is a transition from normal rolls to ob-

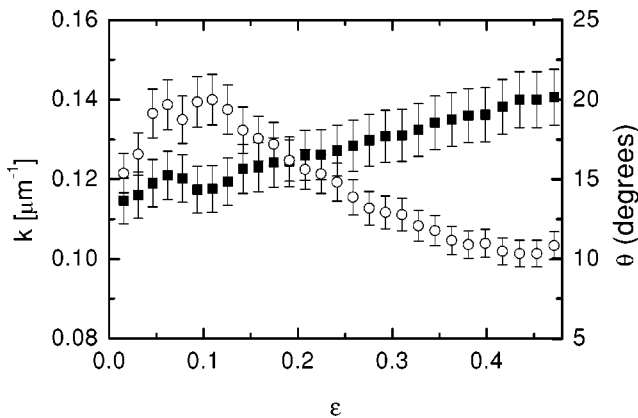


FIG. 4. The wavenumber k of the zig and zag rolls (left-hand axis, solid squares) and the angle of rolls with respect to the undistorted director θ (right-hand axis, open circles) is plotted as a function of ϵ for an applied frequency of 100 Hz. For clarity, only every fifth data point is shown.

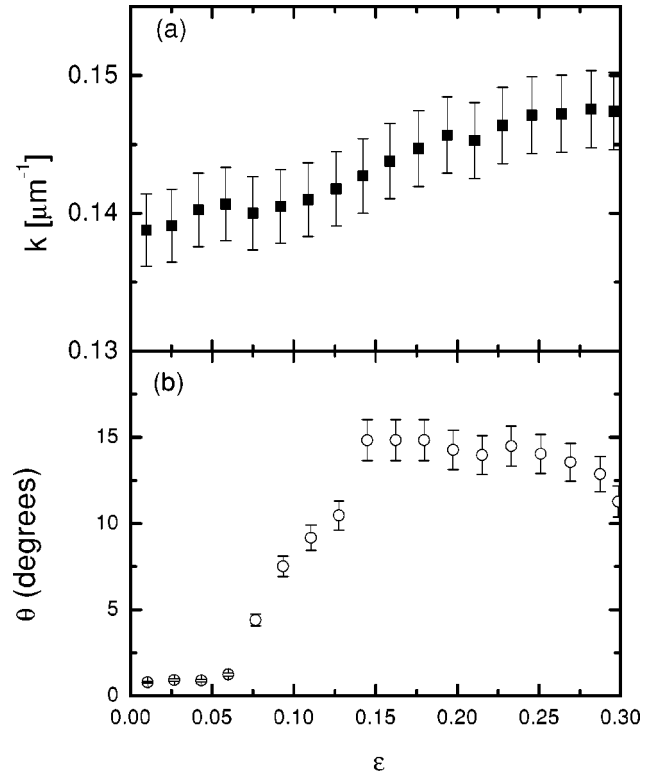


FIG. 5. (a) The wavenumber k of the zig and zag rolls is plotted as a function of ϵ for an applied frequency of 7500 Hz. (b) The angle of rolls with respect to the undistorted director θ is plotted as a function of ϵ for an applied frequency of 7500 Hz. For clarity, in each plot only every tenth data point is shown.

lique rolls as the voltage is increased. This is usually referred to as the zig-zag instability [12,16,33]. The threshold voltage of this transition is determined by measuring the angle θ between the wave vector and the rubbing direction. θ increases continuously from zero as the voltage is increased above the transition. Figure 5 shows both the magnitude of the wave vector and the angle θ as a function of voltage for a particular frequency above the Lifshitz point (7500 Hz). Images of the transition are given in Fig. 6.

The bimodal-varicose instability has been observed in thermoconvection in the nematic liquid crystal 5CB [24] and in electroconvection in I52 [15]. In the latter work, it was originally named the OS2 (oblique roll of the second type) pattern. However, it was clarified in Ref. [16], and shown

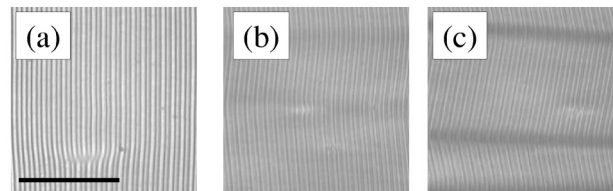


FIG. 6. Three images illustrating the transition from normal rolls to zig zags at an applied frequency of 6500 Hz. The bar in (a) is 0.5 mm and applies to all three images. (a) $V_{rms}=10.9$ V ($\epsilon=2.5 \times 10^{-4}$), (b) $V_{rms}=11.15$ V ($\epsilon=1.5 \times 10^{-3}$), (c) $V_{rms}=11.35$ V ($\epsilon=3.34 \times 10^{-3}$).

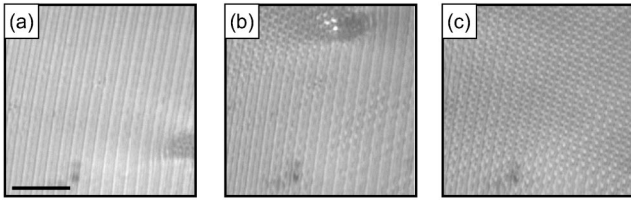


FIG. 7. Three images illustrating the transition from zag rolls to the bimodal-varicose state at an applied frequency of 2000 Hz. The bar in (a) is 0.25 mm and applies to all three images. (a) $V_{rms} = 8.0$ V ($\epsilon = 2.59 \times 10^{-2}$), (b) $V_{rms} = 8.3$ V ($\epsilon = 4.2 \times 10^{-2}$), (c) $V_{rms} = 8.4$ V ($\epsilon = 4.8 \times 10^{-2}$).

definitely in Ref. [17] that the OS2 pattern is equivalent to the bimodal-varicose state. The bimodal-varicose instability is specific to oblique roll patterns. It is due to the growth of a mode with a wave vector that is at an angle of approximately 90° with respect to either the zig or zag rolls that are present in the system.

We observed the bimodal varicose at frequencies less than 6500 Hz. Figure 7 illustrates this transition. As observed in Refs. [15,24], the bimodal-varicose instability nucleates in homogeneous regions that are all zig or all zag and not from grain boundaries between the zig and zag domains. Within a domain of zig or zag rolls, it tends to first appear locally around defects of the pattern. Then, by increasing the voltage, it fills the entire cell.

In Fourier space, the bimodal varicose is detected by a second peak that corresponds to the growing mode. We will follow Ref. [24] and refer to this as the dual wave vector. The onset of the bimodal-varicose regime is calculated by measuring the intensity of this dual peak. The angle θ_{bv} between the bimodal-varicose wave vector and the rubbing direction, and the angle θ_{bd} between the bimodal-varicose wave vector and dual wave vector are plotted in Fig. 8. As mentioned, θ_{bd} is slightly less than 90° . Both angles are decreasing functions of the frequency.

In this paper, we distinguish between two transitions:

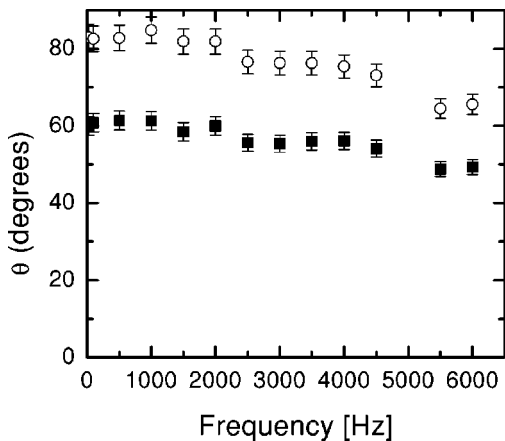


FIG. 8. The angle between the bimodal-varicose wave vector and the dual wave vector (open circles) and the angle between the bimodal-varicose wave vector and the undistorted director (solid squares) as a function of the applied frequency at the onset of the bimodal-varicose state.

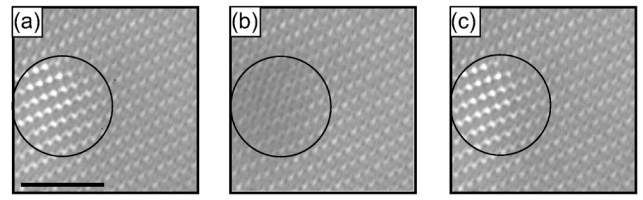


FIG. 9. Three images taken 1.6 s apart illustrating the locally oscillatory bimodal-varicose state. The scale bar in (a) is 0.25 mm and applies to all three images. The circle highlights a region where the oscillation is particularly clear. The applied frequency is 2000 Hz, and the applied voltage is $V_{rms} = 8.46$ V.

bimodal-varicose patterns to oscillating bimodal-varicose patterns and oscillating bimodal-varicose pattern to fully chaotic patterns. The first transition occurs locally, probably near defects as with the initial bimodal-varicose transition. The local oscillatory bimodal varicose is characterized by regions where the relative amplitudes of the zig (or zag) rolls and the dual roll oscillate in time. This state is predicted to exist [16,23], and has been observed in thermoconvection [24] and in electroconvection [17]. The use of the $\lambda/4$ plate highlights this behavior because the initial wave vector and its dual produce twists in the director orientation as a function of z that are opposite each other. Therefore, the overall intensity of the image oscillates as the relative amplitudes of the original mode and the dual mode oscillate. This is illustrated in Fig. 9, where a circle highlights the oscillating region. Upon increasing the voltage, the system enters a state that appears to exhibit spatiotemporal chaos, i.e., irregular behavior in space and time. Figure 10(a) is an image from this regime.

The competition between the zig-zag and skewed-varicose instabilities were studied in detail in Ref. [33]. In this system, we are able to observe a different type of competition: the predicted [12] crossover from the bimodal-varicose instability at low values of the applied frequency to the skewed-varicose instability. The skewed-varicose instability is characterized by undulations in the direction of rub-

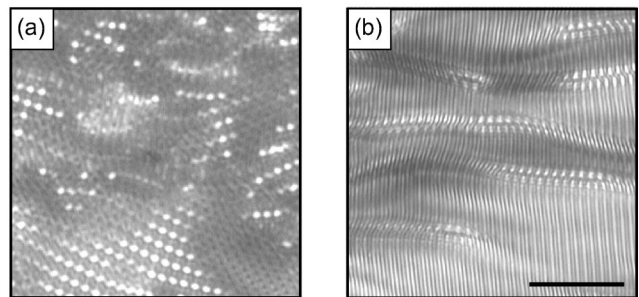


FIG. 10. Comparison of the fully chaotic regime reached via the bimodal-varicose instability with the state existing above the skew-varicose instability. The scale bar in (b) is 0.25 mm and applies to both images. (a) Chaotic state at a driving frequency $f = 1500$ Hz and driving voltage $V_{rms} = 8.4$ V ($\epsilon = 6.63 \times 10^{-2}$). The bimodal nature is visible in the underlying grid pattern. (b) State above the skew-varicose instability for a driving frequency of $f = 8000$ Hz and driving voltage $V_{rms} = 15.8$ V ($\epsilon = 3.7 \times 10^{-2}$).

bing as shown in Fig. 10(b). These undulations have a slow, not completely periodic, back and forth movement. The number of undulations per area increases dramatically with increasing ϵ . The difference between the bimodal varicose (in which the pattern is dominated by a grid-like appearance) and the skew varicose is made clear by comparing Figs. 10(a) and 10(b). The transition between the two instabilities occurs around an applied frequency of 7000 Hz (see Fig. 2). It is interesting to note that as one approaches the transition from lower frequencies, the range of existence of both the bimodal-varicose and the regular, oscillating biomodal-varicose states decreases as a function of ϵ . The behavior right at the transition certainly requires further study, as it appears that up to four transition are converging on a single point.

The transition from a bimodal-varicose instability to a skew-varicose instability is predicted to occur at $\omega\tau_o = 2.8$ ($\tau_o = \epsilon_o\epsilon_{\perp}/\sigma_{\perp}$) for the material parameters of phase 5 [12]. The Lifschitz transition is also predicted to occur at $\omega\tau_o = 0.8$. The material properties of N4 are close to that of phase 5. In our experiments, the Lifschitz and bimodal-varicose-skewed-varicose transitions occurred, respectively, around 2000 and 7000 Hz, which corresponds to $\omega\tau_o$ of 0.4 and 1.4, respectively. There is a factor of 2 between the predicted transition and the measured transition, but the very interesting point is that the ratio between the frequency of transition bimodal varicose/skewed varicose and the Lifschitz frequency are exactly the same in the experiment and in the theory.

IV. SUMMARY

We provide a comprehensive overview of the pattern state diagram for electroconvection in N4 as a function of the applied voltage and frequency. Most of the patterns in electroconvection in N4 have been previously identified in other systems. What is particular to samples of N4 is the transitions between patterns that can be studied and the possibilities for quantitative tests of various theoretical models. First, we find that a comparison of V_c and θ with theoretical curves based on the standard model of electroconvection [21] provides a good estimate of the material parameters for this liquid crystal. Second, the qualitative features of the secondary bifurcations are in agreement with extensions to the standard model that include a twist mode [16]. The next step is to use this pattern state diagram as a quantitative test of this extended model, as the parameters are well determined by the onset behavior. It should be noted that the work in Ref. [17] was also in qualitative agreement with predictions

from calculations using an active twist mode. However, there were quantitative disagreements due to complications from an initial Hopf bifurcation. Such complications do not exist for this system. However, there is one potential quantitative disagreement that needs further testings: the factor of 2 between the predicted and observed value for the Lifschitz frequency and the value for the transition from bimodal varicose to skew varicose.

The transition from bimodal varicose to skew varicose is a particularly interesting new characteristic of the pattern state diagram for N4. One would expect interesting pattern formation near the point where the two instabilities meet. Also, one needs to map out the transition between the two states for values of the voltage above the bimodal and (or) skew varicose transition as a function of frequency. A detailed study of this region will be the subject of future work.

Finally, there remain open questions that have originated in the theoretical analysis of the twist mode and abnormal rolls that may be addressable with this system. First, there is the possibility of hysteresis as a function of applied frequency between abnormal rolls and oblique rolls [12]. We did not observe abnormal rolls under the conditions reported on in this paper; however, they were found to exist at lower conductivities. This will be the subject of future work. Also, the state of apparent spatiotemporal chaos that exists at low frequency above the oscillating bimodal-varicose instability deserves further study. The connections between the local, oscillating bimodal-varicose state and the “chaotic” state needs to be clarified. Also, the role of all three modes (original wave vector, dual wave vector, and twist mode) in the dynamics of this state needs to be studied. Finally, the issue of controlling, or eliminating, this state of spatiotemporal chaos is of interest. For the case of traveling rolls, temporal modulation is known to be able to eliminate spatiotemporal chaos by coupling the left- and right-traveling rolls [34]. Therefore, it will be useful to explore the impact of temporal modulation on this state, for which a fundamental frequency exists, but for which the rolls are not traveling rolls.

ACKNOWLEDGMENTS

We thank Emmanuel Plaut, Werner Pesch, and Guenter Ahlers for useful discussions. This work was supported by NSF Grant No. DMR-9975479. M. Dennin also thanks the Alfred P. Sloan Foundation and the Research Corporation for financial support for this work. B.S. was supported by NSF Research Experience for Undergraduates Grant No. PHY-9988066.

[1] M.C. Cross and P.C. Hohenberg, *Rev. Mod. Phys.* **65**, 851 (1993).
 [2] L. Kramer and W. Pesch, *Annu. Rev. Fluid Mech.* **27**, 515 (1995).
 [3] P.G. de Gennes and J. Prost, *The Physics of Liquid Crystals* (Clarendon Press, Oxford, 1993).
 [4] S. Kai and K. Hirakawa, *Prog. Theor. Phys.* **64**, 212 (1978).

[5] A. Joets, X.D. Yang, and R. Ribotta, *Physica D* **23**, 235 (1986).
 [6] I. Rehberg, S. Rasenat, J. Fineberg, M. de la Torre Juárez, and V. Steinberg, *Phys. Rev. Lett.* **61**, 2449 (1988).
 [7] M. Dennin, M. Treiber, L. Kramer, G. Ahlers, and D.S. Cannell, *Phys. Rev. Lett.* **76**, 319 (1996).
 [8] I. Rehberg, S. Rasenat, and V. Steinberg, *Phys. Rev. Lett.* **62**, 756 (1989).

- [9] A. Joets and R. Ribotta, *Phys. Rev. Lett.* **60**, 2164 (1988).
- [10] M. Dennin, G. Ahlers, and D.S. Cannell, *Phys. Rev. Lett.* **77**, 2475 (1996).
- [11] H.R. Brand, C. Fradin, P.L. Finn, W. Pesch, and P.E. Cladis, *Phys. Lett. A* **235**, 508 (1997).
- [12] E. Plaut, W. Decker, A.G. Rossberg, L. Kramer, W. Pesch, A. Belaidi, and R. Ribotta, *Phys. Rev. Lett.* **79**, 2367 (1997).
- [13] J.H. Huh, Y. Hidaka, and S. Kai, *Phys. Rev. E* **58**, 7355 (1998).
- [14] S. Kai, K. Yamaguchi, and K. Hirakawa, *Jpn. J. Appl. Phys.* **14**, 1635 (1975).
- [15] M. Dennin, D.S. Cannell, and G. Ahlers, *Phys. Rev. E* **57**, 638 (1998).
- [16] E. Plaut and W. Pesch, *Phys. Rev. E* **59**, 1747 (1999).
- [17] M. Dennin, *Phys. Rev. E* **62**, 6780 (2000).
- [18] H. Richter, A. Buka, and I. Rehberg, *Phys. Rev. E* **51**, 5886 (1995).
- [19] M. Dennin, G. Ahlers, and D.S. Cannell, *Science* **272**, 388 (1996).
- [20] Y. Hidaka, J.H. Huh, K.I. Hayashi, S. Kai, and M.I. Tribelsky, *Phys. Rev. E* **56**, R6256 (1997).
- [21] E. Bodenschatz, W. Zimmermann, and L. Kramer, *J. Phys. (France)* **49**, 1875 (1988).
- [22] M. Treiber and L. Kramer, *Mol. Cryst. Liq. Cryst. Suppl. Ser.* **261**, 311 (1995).
- [23] E. Plaut and R. Ribotta, *Eur. Phys. J. B* **5**, 265 (1998).
- [24] E. Plaut, L. Pastur, and R. Ribotta, *Eur. Phys. J. B* **5**, 283 (1998).
- [25] E. Industries, Tech. Doc. Rep. ARL TDR, 2001 (unpublished).
- [26] J. S. Martin and S. Garg (private communication).
- [27] K.S.H. Knepe and N. Sharma, *J. Chem. Phys.* **77**, 3203 (1982).
- [28] M. Dennin, Ph.D. thesis, U. C. Santa Barbara, 1995.
- [29] The calculation of the critical voltage and angle used a program supplied by Werner Pesch.
- [30] A.B.M. Treiber, N. Eber, and L. Kramer, *J. Phys. II* **7**, 649 (1997).
- [31] H. Amm, R. Stannarius, and A.G. Rossberg, *Physica D* **126**, 171 (1999).
- [32] S. Rasenat, G.H.B.L. Winkler, and I. Rehberg, *Exp. Fluids* **7**, 412 (1989).
- [33] S. Nasuno, O. Sasaki, S. Kai, and W. Zimmermann, *Phys. Rev. A* **46**, 4954 (1992).
- [34] M. Dennin, *Phys. Rev. E* **62**, 7842 (2000).